

PAPER • OPEN ACCESS

Tomographic reconstructions of the MAST-U fast ion loss detector using iterative algorithms

To cite this article: M Jimenez-Comez *et al* 2025 *Plasma Phys. Control. Fusion* **67** 125005

View the [article online](#) for updates and enhancements.

You may also like

- [Edge fluctuation measurements in EDA H-mode and QCE plasmas in ASDEX Upgrade using the correlation electron cyclotron emission diagnostic](#)
J Schellpfeffer, B Vanovac, M Faitsch et al.
- [Investigation of the fast ion driven kinetic ballooning mode in FIRE mode discharge through gyrokinetic simulations](#)
D Kim, B J Kang, S J Park et al.
- [Statistical inference of anomalous thermal transport with uncertainty quantification for interpretive 2D SOL models](#)
Y Fu, B Dudson, X Chen et al.

Tomographic reconstructions of the MAST-U fast ion loss detector using iterative algorithms

M Jimenez-Comez¹ , B Schmidt² , J Rueda-Rueda^{2,*} , L Velarde³ ,
J F Rivero-Rodriguez⁴ , A Reyner-Vinolas¹ , M Garcia-Munoz¹ , J Gonzalez-Martin⁴ ,
E Viezzer¹ , the MAST Upgrade Team⁵ and the EUROfusion Tokamak Exploitation Team⁶

¹ Department of Atomic, Molecular and Nuclear Physics, University of Seville, Seville, Spain

² Department of Physics and Astronomy, University of California Irvine, Irvine, CA, United States of America

³ Department of Energy Engineering, University of Seville, Seville, Spain

⁴ Department of Mechanical and Manufacturing Engineering, University of Seville, Seville, Spain

E-mail: jruedaru@uci.edu

Received 30 September 2025, revised 12 November 2025

Accepted for publication 27 November 2025

Published 5 December 2025



CrossMark

Abstract

In this work, we evaluate the Kaczmarz, Coordinate descent, and Cimmino algorithms together with the resolution principle as stopping criteria, using a synthetic signal model for the MAST-U fast-ion loss detector (FILD), complementing the efforts recently done for the ASDEX Upgrade FILD. The performance of these algorithms is assessed by analyzing the evolution of the reconstruction error as well as the computation time. To further assess the reliability of the reconstructions, a ‘fidelity map’ that reconstructs signals at each grid point is introduced to visualize reconstruction accuracy across velocity space. The Kaczmarz algorithm, which shows better performance in terms of accuracy, is also applied to experimental MAST-U FILD measurements of prompt fast-ion losses in an L-mode plasma heated by an on-axis neutral beam injector with 1.5 MW of input power. This algorithm demonstrates improved performance compared to 0th-order Tikhonov regularization.

Keywords: tomography, fast ions, fast ion loss detector

⁵ See Harrison *et al* 2024 (<https://doi.org/10.1088/1741-4326/ad6011>) for the MAST Upgrade Team.

⁶ See Joffrin *et al* 2024 (<https://doi.org/10.1088/1741-4326/ad2be4>) for the EUROfusion Tokamak Exploitation Team.

* Author to whom any correspondence should be addressed.



Original Content from this work may be used under the terms of the [Creative Commons Attribution 4.0 licence](https://creativecommons.org/licenses/by/4.0/). Any further distribution of this work must maintain attribution to the author(s) and the title of the work, journal citation and DOI.

1. Introduction

Undesired transport of fast ions is often associated with different instabilities, such as toroidal Alfvén eigenmodes [1] or Edge localized modes (ELMs) [2, 3], which can significantly impact plasma performance [4–6]. These instabilities induce anomalous transport, altering the fast-ion phase-space distribution and leading to the loss of confinement of part of the fast-ion population. The resulting localized fluxes of heat and particles to plasma-facing components pose a serious threat to the integrity of fusion reactors [7]. Gaining insight into the mechanisms driving instability-induced transport, as well as developing effective control strategies [8], requires detailed information on the velocity-space distribution of fast-ion losses. The fast-ion loss detector (FILD) [9] is a diagnostic specifically designed to measure these losses, providing valuable data on the velocity-space distribution of escaping fast ions.

Positioned within the tokamak, along the vessel wall, the FILD detector works like a magnetic spectrometer, using the local magnetic field to guide fast ions onto a scintillator. The scintillator emits light at the strike position of the fast ion, which depends on its energy and pitch. Hence, FILD cannot resolve different particles with the same charge-to-mass ratio, for instance, D and ^4He . The emitted light from the scintillator plate is guided by a series of lenses and directed towards the acquisition system: a high-resolution camera and a fast acquisition system. A representation of the operational principle, along with a 3D computer-aided design of the essential components within the detector head can be seen in figure 1 of [10]. A detailed description of the FILD working principle and its typical resolutions and synthetic diagnostic can be found in [11]. FILDs have been implemented in a wide range of machines such as TFTR [9, 12, 13], ASDEX Upgrade [14–16], JET [17–19], DIII-D [20], KSTAR [21, 22], EAST [23–25] and TCV [26, 27]. MAST-U had a FILD installed as part of the machine upgrade [28].

FILD measurements are characterized by two variables: gyroscalar ρ and pitch angle α [29–31]. Let I_p be the plasma current and B_t the on-axis toroidal magnetic field, we can define

$$\rho = \frac{mv}{qB} \quad (1)$$

$$\cos \alpha = \text{sgn}(I_p B_t) \frac{v_{\parallel}}{v} \quad (2)$$

where m and q are the mass and charge of the ion, B is the magnetic field, $v = \sqrt{v_{\parallel}^2 + v_{\perp}^2}$ is the total velocity, v_{\parallel} is the parallel velocity and v_{\perp} is the perpendicular velocity with respect to the magnetic field.

However, the measured velocity-space distribution suffers from distortion due to resolution limitations. Therefore, it is necessary to apply signal processing techniques, such as tomographic reconstruction, that allow obtaining an undistorted fast-ion velocity-space distribution. In particular, tomographic techniques applied to FILD have played an important role in determining the velocity-space structures of fast-ion acceleration during ELMs [32, 33]. Tikhonov regularization has

so far been the method par excellence applied to FILD measurements [11, 30, 31]. However, it presents some drawbacks. It is dominated by a hyperparameter whose value is critical to the result. The methods available to choose the optimal value for this hyperparameter are partially manual, and selecting a suboptimal value can lead to oversmoothed solutions or contamination by noise. Also, it is computationally expensive. Depending on the size of the matrices used, a scan of 10 hyperparameters can take from 0.5 to 24 hours per frame when changing the grid size a 13% in the scintillator space and another 13% in the pinhole space. This calculation was done in an architecture of x86_64 (64-bit), Intel Xeon Gold 6248R, 10 cores. In search of more efficient methods, iterative-based algorithms have been proposed and tested in the ASDEX Upgrade (AUG) FILD. These algorithms use a stopping criterion known as the resolution principle, which is based on the method's ability to distinguish between peaks [29]. Here, we extend this work by evaluating the three proposed iterative algorithms, Kaczmarz [34, 35], Coordinate descent [36–38] and Cimmino [39], for the MAST-U FILD [10]. As a spherical tokamak, MAST-U presents specific tomographic-relevant characteristics that differ from those of ASDEX Upgrade, necessitating an investigation into the behavior of iterative reconstruction methods on this machine. One of the key differences that MAST-U exhibits is a broader range of fast-ion gyroscalars (from 9 to 15 cm while in AUG is usually from 2 to 6 cm) [10, 40]. This wider range requires faster and more efficient computational methods to perform real-time or near real-time tomographic reconstructions. Additionally, FILD diagnostic resolution deteriorates for larger gyroscalars, making the interpretation of the measurements challenging, as signals corresponding to nearby gyroscalars can become difficult to distinguish. This fact makes tomography especially important in the MAST-U FILD.

The drawbacks of traditional Tikhonov regularization motivate this work's investigation of iterative reconstruction methods. In our application, these methods offer clear practical and scientific advantages. First, they are orders of magnitude faster (seconds per frame rather than minutes or hours), enabling analysis of fast-ion dynamics of entire discharges rather than static snapshots. Second, they resolve the primary workflow bottleneck of hyperparameter selection: unlike Tikhonov, which requires a full computation for each value of the regularization parameter, iterative methods build a solution path $x^{(1)}, x^{(2)}, \dots$ from which the optimal iterate can be selected post hoc. Third, they provide an implicit, adaptive regularization that refines from coarse to fine scales, reducing the uniform oversmoothing characteristic of Tikhonov regularization and improving separation of nearby features when present in the data. This adaptive behavior is controlled by physically-motivated criteria—here the resolution principle—which selects the iteration before noise-dominated artefacts appear and has been validated on synthetic and experimental fast-ion measurements.

This paper is organized as follows. Section 2 describes the mathematical framework for FILD measurements and tomography. The MAST-U FILD resolution is characterized in

sections 3 and 4 solves the inverse problem with the iterative algorithms for a synthetic signal of the MAST-U FILD. Likewise, to identify the regions of the phase-space in which the reconstructions present more reliability, that is, less error, a fidelity map has been developed and is presented in section 5. This map consists of performing systematic reconstructions of each point in the domain and evaluating its error. In this way, a visual representation of the reliability of the tomography is obtained. The resolution principle as stopping criteria is described in section 6. In addition, an updated version of the construction of resolution maps needed for its application is also presented in section 6. The implementation of the iterative methods together with the resolution principle has been standardized and included in the open-source FILDSIM workflow code [11, 41, 42]. In section 7, the developed software is applied to an experimental MAST-U case from the first analysis of the velocity-space of fast-ion losses [40]. The performance of the Kaczmarz algorithm together with the resolution principle is compared to the 0th-order Tikhonov regularization algorithm. Finally, section 8 concludes the paper.

2. FILD modeling and reconstructions

Following the modeling of FILD measurements, tomographic techniques can be applied to reduce the distortion that these measurements suffer due to the limits of diagnostic resolution.

2.1. Mathematical modeling of the FILD measurements

Let $V \subset \mathbb{R}^2$ be the velocity space defined by the gyroscalar ρ and pitch angle α . Let $S \subset \mathbb{R}^2$ represent the scintillator plate that is described by some coordinate system (c_1, c_2) . It is shown that the scintillator signal can also be interpreted by the variables gyroscalar and pitch. Suppose a collection of N particles at the pinhole plane with a given gyroscalar $\rho = \rho'$ and pitch angle $\alpha = \alpha'$. This set of particles have random initial positions and gyrophases, within the pinhole plane. Therefore, the particles will reach the scintillator at different positions following a distribution. The spot formed by the striking particles can be labeled with the coordinate of its centroid (c_1^C, c_2^C) . Now, repeating the process for other values of (ρ', α') , a mapping ψ called *strike-map* [11] can be defined to associate (c_1^C, c_2^C) with the phase-space variables.

$$\psi: S \rightarrow V \quad (3)$$

$$(c_1^C, c_2^C) \mapsto (\rho', \alpha'). \quad (4)$$

In this way, a FILD camera frame showing the distribution of the ions in the real space of the scintillator can be remapped to velocity-space coordinates. The FILD signal represented in terms of gyroscalar and pitch angle is known as *remap*.

Notice that for a collection of N particles initialized at the pinhole with fixed (ρ, α) , the distribution formed in the scintillator covers a subset of the scintillator surface. Its remap into velocity space variables will return a distribution that apparently covers a range of gyroscalar and pitch angle values. To distinguish between these two representations, primed

variables (ρ', α') are usually used to describe the measured velocity-space distribution, and unprimed variables (ρ, α) for the true velocity-space distribution.

With this distortion in the measurements it is not possible to directly measure the gyroscalar and pitch at the pinhole with the measurements obtained in the remap. However, measurements obtained $\mathcal{M}_s(\rho, \alpha)$ can be related to the velocity-space distribution at the pinhole $f_p(\rho, \alpha)$ in terms of a weight function $W(\rho', \alpha', \rho, \alpha)$ [11, 30] as done in other diagnostics [43–45].

$$\mathcal{M}_s(\rho, \alpha) = \int_0^{2\pi} d\alpha' \int_0^\infty W(\rho', \alpha', \rho, \alpha) f_p(\rho, \alpha) d\rho'. \quad (5)$$

2.2. Forward problem

Equation (5) can be discretized using a midpoint quadrature rule [43]. Let $y \in \mathbb{R}^m$ be the discretized measurements at the scintillator, $x \in \mathbb{R}^n$ be the original signal at the pinhole, and $A \in \mathbb{R}^{m \times n}$ be the weight function. The matrix form of equation (5) can be expressed as

$$y = Ax. \quad (6)$$

The forward problem consists in obtaining y for a given discrete fast-ion distribution at the pinhole x knowing A . This process is done by the FILD experimental setup when taking measurements.

2.3. Inverse problem

The aim of the inverse problem is to recover x from equation (6) knowing the FILD remap and the weight matrix. This is an ill-posed problem that can be solved with various techniques [46]. The most widely used method for FILD tomography is 0th order Tikhonov regularization [11, 29–31]. The optimization problem addressed by Tikhonov method is the following.

$$\min_x \|Ax - y\|^2 + \lambda \|Lx\|^2 \quad (7)$$

where L is the regularization matrix, λ is a hyperparameter that determines the weight of the regularization and $\|\cdot\|$ represents the euclidean norm. The minimization problem (7) has a direct solution \hat{x}_λ that explicitly depends on λ .

$$\hat{x}_\lambda = (A^T A + \lambda L^T L)^{-1} A^T y. \quad (8)$$

An automated and robust procedure for computing the hyperparameter is yet unavailable. However, there are techniques to facilitate the choice, such as the L -curve method [47, 48]. In the 0th order Tikhonov regularization, the problem is simplified by taking L as the identity matrix. Non-negativity constrain can be added to ensure physically relevant solutions. This version of the method is called non-negative Tikhonov regularization.

2.4. Tomographic iterative algorithms

If after the reconstruction using Tikhonov, the selected λ does not turn out to be appropriate, then the computation has to be restarted with a new hyperparameter value. To overcome these difficulties, iterative algorithms have been proposed as alternative methods. Kaczmarz, Coordinate descent, and Cimmino algorithms are three iterative algorithms tested in ASDEX Upgrade FILD [29] that have returned promising results in terms of speed and reconstruction quality. Their estimated solution \hat{x}^{k+1} is calculated with simple projections using the result of the previous iteration k . This reduces computational cost and prevents restarting the reconstruction from scratch to test a new hyperparameter value.

The Kaczmarz algorithm [34, 35] is a row-action method, where each iteration consists of a cyclic process that sequentially selects the rows of the weight matrix $A = A_{ij}$ where i runs over the pinhole index and j in the scintillator space. Each selected row A_i is used to project the current estimated solution onto the hyperplane defined by A_i and the i th element of the vector y . Coordinate descent [36–38], as an example of column-action method, applies the same principle of cyclic projections but using the columns of A . In this case, an element of the solution \hat{x}^k is updated based on the summed errors of the projections that affect it. In the Cimmino algorithm [39], projections are performed simultaneously on all hyperplanes.

The sequence of updated solutions $\{\hat{x}^{(k)}\}$ generated by these algorithms will ideally converge to a solution \hat{x} for the inverse problem. In practice, however, it is not possible to compute an infinite number of iteration, so a stopping condition must be defined. Furthermore, in the presence of noise, computing too many iterations is undesirable, as iterates will eventually begin to amplify measurement noise rather than refine the signal (a well-known phenomenon called semi-convergence), implying that a stopping criteria must be employed [49]. Taking these considerations into account, the maximum number of iterations k_{\max} can be treated as a hyperparameter. However, its selection is not as critical as that of λ in Tikhonov because recalculation is not required. In this case, the solution is built sequentially. Therefore, all intermediate iterations can be stored for review. If further iterations are needed, the last calculated iteration can be given as starting point for the iterative algorithm.

3. MAST-U FILD characterization

MAST-U [50] has two neutral beam injectors as external fast ion sources: an on-axis NBI, called south-south due to its location and injection direction (SS Beam); and an off-axis NBI, called south-west (SW Beam) for similar reasons. The birth spatial distribution of energetic ions injected by these beams is depicted in figure 1. Deuterium is typically injected at energies ranging from 50 to 75 keV.

As explained in section 2, the measurements obtained by FILD present a broadening relative to the point from which they originate in the pinhole. These dispersions σ_α and σ_ρ in α and ρ directions are not uniform, but depend on the specific values of α and ρ . The study of the dispersion can be

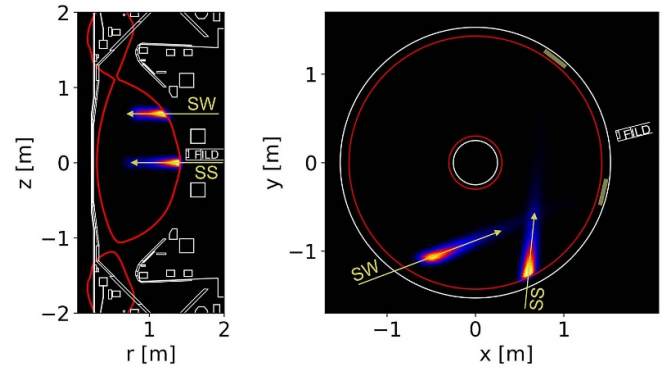


Figure 1. Poloidal (left) and toroidal (right) cross sections of MAST-U, showing the birth profiles of the on-axis (SS) and off-axis (SW) beams, along with the FILD position and the separatrix (in red). Reproduced from [40]. © The Author(s). Published by IOP Publishing Ltd. [CC BY 4.0](https://creativecommons.org/licenses/by/4.0/).

performed by initializing ions at the pinhole with FILDSIM and tracing their trajectory to the scintillator. These trajectories will depend on the orientation of the magnetic field. This orientation is defined by the rotation angles θ and ϕ , which allows to transform from a reference system where the magnetic field is aligned with the z -axis with one where the normal to the FILD pinhole plane is aligned with the z -axis. The angles are defined such as if $(\theta = 0^\circ, \phi = 0^\circ)$ the magnetic field is contained in the pinhole plane and is parallel to the scintillator plate. A complete description of how this transformation is implemented in FILDSIM can be found in the documentation of the routine `getBangLes()` from the ScintSuite package [41] used to launch FILDSIM.

In previous analysis [40], it was shown that when the magnetic field is perfectly aligned with the probe head ($\theta = 0^\circ, \phi = 0^\circ$), larger gyroscalars result in larger dispersion. This occurs because the collimator has less effect on these gyroscalars values. Here, we quantify the effects of changes in the magnetic field orientation by scanning values of θ and ϕ which encompass the values observed in shot #47132, a reference discharge for fast-ion studies in the second MAST-U experimental campaign. The instrument response has been obtained a recently upgraded FILDSIM code [51, 52] following 10^6 markers for each pair of gyroscalar-pitch in a set of 19 different values of ρ , ranging from 3.5 to 21 cm (~ 5 to 182 keV for a typical magnetic field at the FILD head of 0.415 T and deuterium assumed as the measured ion), and a set of 13 values of α , ranging from 25 to 85° as typical MAST-U FILD range of pitch angle. Figure 2 shows a scan in $\theta \in [-12, 0]$ degrees for $\phi = 0^\circ$ and figure 3 shows a scan in $\phi \in [-12, 0]$ degrees for $\theta = 0^\circ$. Both scans correspond to $\rho = 12.4$ cm and $\alpha = 60^\circ$, representative values for the on-axis NBI signal [40]. Variations in dispersion are observed to be within the error bars. Hence, small uncertainties in the field orientation due to uncertainties in the equilibrium reconstruction will not have a significant effect in the calculation of the weights functions nor in the performed tomographic reconstructions.

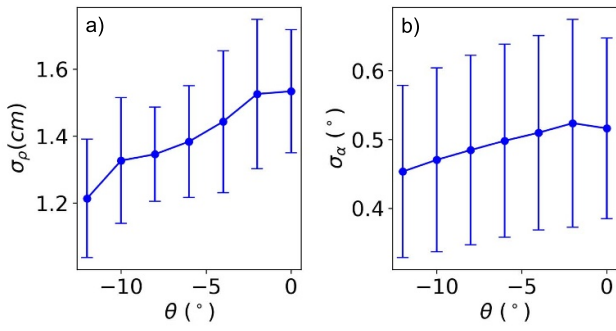


Figure 2. Scan in θ for (a) gyroscalar and (b) pitch angle resolution $\sigma_\rho, \sigma_\alpha$ for $\phi = 0^\circ$ and $\rho = 12.4$ cm and $\alpha = 60^\circ$.

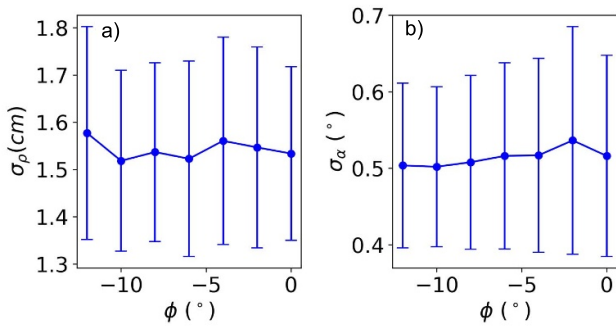


Figure 3. Scan in ϕ for the (a) gyroscalar and (b) pitch angle resolution $\sigma_\rho, \sigma_\alpha$ for $\theta = 0^\circ$ and $\rho = 12.4$ cm and $\alpha = 60^\circ$.

4. Inverse problem: synthetic model

The first phase-space analysis for the MAST-U FILD [40] focused first on discharges with only prompt losses, where the energy associated to the measured gyroscalar would match the NBI injection energy within diagnostic resolution. In particular, discharges using only one beam were considered to better characterize the losses of each injector. To apply and develop iterative methods, we will rely on the on-axis beam experimental case presented in [40]. The measured signal associated with the main energy of the NBI shows a split across several pitch angle values, and the goal is to resolve the energy corresponding to each of the collected peaks.

A synthetic MAST-U signal is calculated as a test distribution for the inverse problem based on the shot #47132 for time $t = 0.30$ s where the on-axis NBI is present with $E = 62.8$ keV. The weight matrix used has 66×176 grid size for the scintillator (66 grid points for pitch angle and 176 for gyroscalar) and 66×146 (66 grid points for pitch angle and 146 for gyroscalar) for the pinhole with a resolution of 1° in pitch and 0.1 cm in gyroscalar to ensure that the resolution employed is sufficient to resolve the physical phenomena of interest. These discretizations for the pinhole (solution space) and scintillator (measurement space) are kept identical for both the forward and inverse problems. For the weight matrix calculation, it was considered that the scintillator efficiency has a linear behavior

in the range of energies that are measurable with the FILD as done in [53].

The first step to build a synthetic model for FILD is to build a synthetic pinhole fast-ion distribution x . For this purpose Gaussian distributions are used. This is $\rho \sim N(\rho_0, \sigma_\rho^2)$ and $\alpha \sim N(\alpha_0, \sigma_\alpha^2)$. A single spot is modeled as a multi-Gaussian of independent variables with mean $\mu_x = (\rho_0, \alpha_0)$ and covariance $C_x = \begin{pmatrix} \sigma_\rho^2 & 0 \\ 0 & \sigma_\alpha^2 \end{pmatrix}$. The discrete signal x is generated first as the sums of various multi-Gaussian distributions to mimic different NBI energies. Once the array is created, a threshold is applied to its pixels to remove values far from the spot location. In this way, it is possible to obtain defined spots without noise.

$$x_i = \begin{cases} x_i & \text{for } x_i \geq 0.001x_{\max} \\ 0 & \text{for } x_i < 0.001x_{\max} \end{cases}$$

Now, x is multiplied by the weight matrix A to calculate the associated measurements y . However, real measurements contain noise induced by the experimental setup. Let m_1 and m_2 be the scintillator's dimensions in pitch angle and gyroscalar respectively. To improve the synthetic model, noise $\epsilon \in \mathbb{R}^{m_1 \times m_2}$ composed of signal noise ϵ_1 and background noise ϵ_2 is added to the signal. A Gaussian array $n \in \mathbb{R}^{m_1 \times m_2}$ of mean 0 and sigma 1, is defined. From it, the signal noise is defined as $\epsilon_1 = \sigma_1(y * n)$ where σ_1 acts as the percentage of noise applied and the product is performed element by element. The idea is to apply noise in the scintillator signal area taking into account the value of each pixel, to mimic the experimental photon noise. In contrast, $\epsilon_2 = \sigma_2 \cdot y_{\max} \cdot n$ where σ_2 gives the level of background noise applied. Finally, $\epsilon = \max\{\epsilon_1, \epsilon_2\}$. Let \bar{y} be the noisy synthetic measurement. By definition it is satisfied that

$$\bar{y} = Ax + \epsilon \quad (9)$$

Consider the injection energies $E_1 = 62.8$ keV, $E_2 = 31.4$ keV, and $E_3 = 20.9$ keV and a magnetic field at the FILD head of 0.414 T. The corresponding gyroscalar positions that will serve as means for the multi-gaussians are 12.4 cm, 8.8 cm, and 7.2 cm. Signal intensities of 70%, 20%, and 10% can be assumed, respectively. As an on-axis distribution is considered, the selected pitch angle is 60° . Finally, to recover similar deviations in the scintillator as in experiments, the standard deviations in the pinhole are set to $\sigma_\rho = 0.45$ and $\sigma_\alpha = 0.1$. This resolution in pitch angle is set since a discrete pitch signal is expected. An illustration of the resulting distribution can be seen in figures 4(a) and (b).

The test of the iterative algorithms is started by performing ideal inversions of the synthetic scintillator data. That is, solving the inverse problem without adding noise. Later, the algorithms are tested with noisy synthetic signal. To implement noise, $\sigma_1 = 0.1$ and $\sigma_2 = 0.01$ are used. This analysis will be employed to select the best algorithm for the MAST-U FILD tomography.

The performance of these algorithms is evaluated with the increase in computation time with increasing number of iterations and with the reconstruction error ϵ . This metric is defined

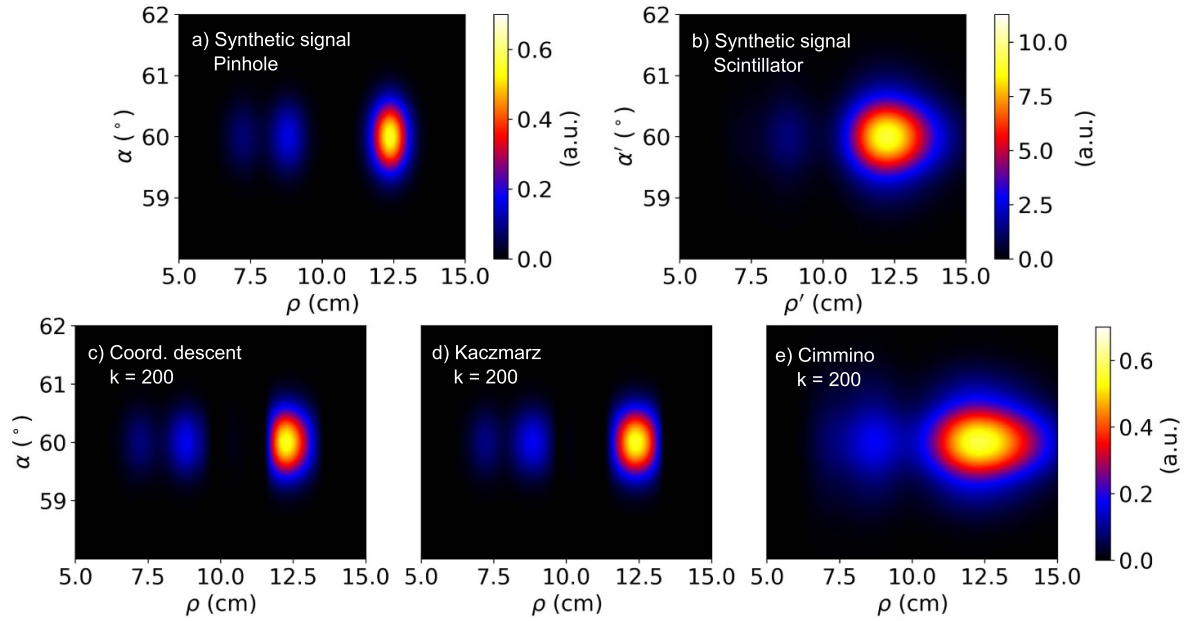


Figure 4. a) Synthetic pinhole distribution for MAST-U on-axis NBI (b) Synthetic Scintillator signal (c) Coordinate descent reconstruction for $k = 200$ (d) Kaczmarz reconstruction for $k = 200$ (e) Cimmino reconstruction for $k = 200$.

using the l_2 norm [48]:

$$\varepsilon = \frac{\|x - \hat{x}\|}{\|x\|}. \quad (10)$$

4.1. Ideal inversions

Reconstruction examples of the three algorithms for $k = 200$ can be found in figures 4(c)–(e). It is observed that Coordinate descent and Kaczmarz algorithms return a signal similar to the synthetic signal in the pinhole. However, Cimmino algorithm does not improve the signal present in the scintillator. The evaluation of the algorithms metrics can be found in figure 5. The Kaczmarz algorithm demonstrates strong performance in terms of reconstruction error. However, Coordinate descent presents a more favorable trend in computational time with respect to iteration scalability. It can run a larger number of iterations in a shorter time. This characteristic makes it a suitable candidate for preliminary analysis of FILD data in scenarios where the optimal number of iterations has not yet been established. The metrics in figures 5(a) and (b) show that while the Cimmino algorithm has the lowest computation time per iteration, it returns a significantly higher reconstruction error. An analysis of the convergence behavior of the three algorithms, as shown in figure 5(c), reveals that Cimmino converges at a much slower rate and stabilizes at a higher error level compared to the other algorithms. To illustrate the difference in behavior between the algorithms, iteration $k = 200$ is marked in figure 5(c) for the three curves. While Cimmino still exhibits a high error in $k = 200$, the other two algorithms have already stabilized at a low error level. This is also illustrated in figure 4(e). Furthermore, it can be observed that

Coordinate Descent requires less time to complete 200 iterations than Kaczmarz, whereas Kaczmarz reaches a similar error in fewer iterations. With the presented results, we conclude that Cimmino is not suitable for fast tomography due to its longer convergence time-scale and its reconstruction error level. In contrast, Coordinate descent shows the best error-time per iteration ratio and Kaczmarz the lowest reconstruction error. These two algorithms seem appropriate for tomography, but their robustness against noise must be studied to determine their suitability.

4.2. Noisy signal reconstructions

In this subsection, the noisy formulation of the inverse problem is addressed. The synthetic scintillator signal contains 10% signal noise and 1% background noise, mimicking the experimental signal, which exhibits approximately 1.2% noise relative to its peak value. A reconstruction for $k = 100$ is shown in figure 6. It is clear that artifacts appear on the left side of the image where the edge of the collimator is placed. These artifacts are responsible for significantly increasing the reconstruction error.

To solve this issue, a projection onto the reconstruction region of interest is performed after every iteration. For our case, the signal region is $\rho \in [6.5, 15]$ cm and $\alpha \in [59, 61]$ degrees. Projecting onto the signal region prevents the development of artifacts, as can be seen in figure 6.

The convergence test in figure 7(c) has been repeated for noisy inversions, leading to results presented in figure 7. As in the ideal case, Cimmino performs with a slow convergence rate, Coordinate descent shows the best error-execution time

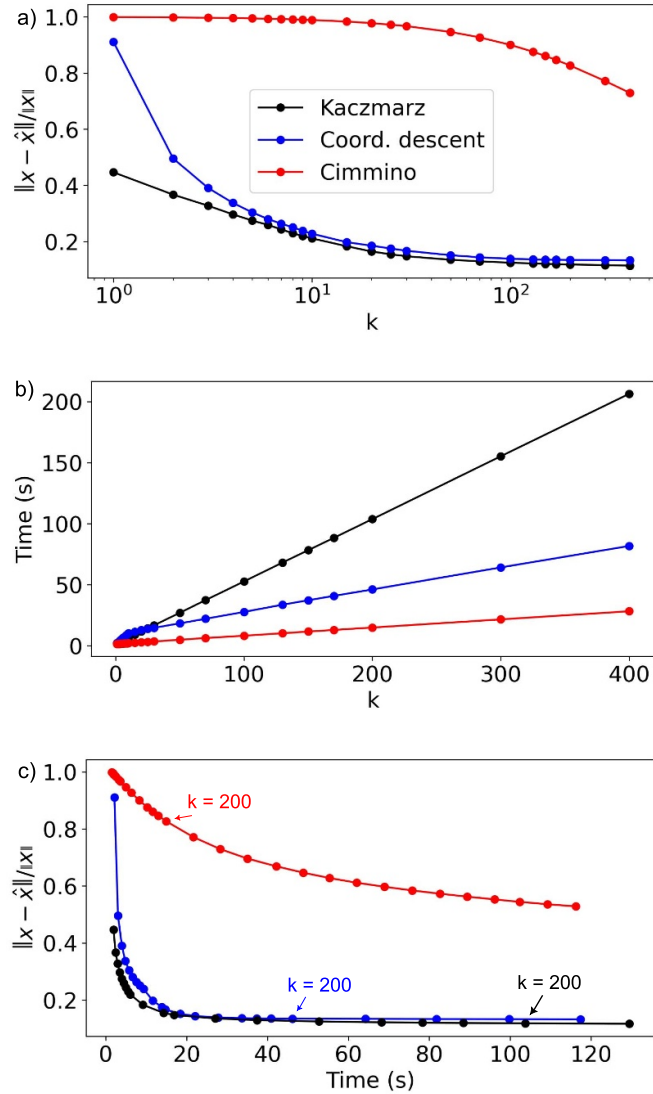


Figure 5. Evaluation metrics for the synthetic ideal inversion. (a) Evolution of the reconstruction error with the number of iterations k . (b) Evolution of the computation time as a function of the number of iterations. The three algorithms show linear dependence between the execution time and the number of iterations. (c) Evolution of the error as a function of time showing the convergence of each algorithm.

ratio and Kaczmarz achieves lower errors than coordinate descent in similar execution time. Hence, Kaczmarz is chosen as the most suitable algorithm for tomographic analysis of the MAST-U FILD. However, Kaczmarz and Coordinate descent algorithms are both suitable for tomography and its choice would depend on the priorities of the analysis.

Notice that the errors associated with Kaczmarz and Coordinate descent start to increase after a minimum is reached slightly after 100 iterations. This phenomenon is known as semi-convergence and is the expected behavior in iterative algorithms when performing noisy reconstructions. Initially, the algorithm tends to an accurate approximation of the solution but eventually it starts to converge into a noisy approximation [49]. Unlike the ideal case, in the noisy case,

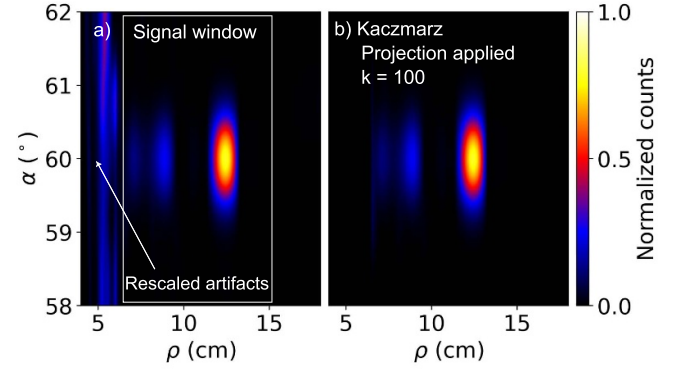


Figure 6. (a) Kaczmarz reconstruction of the noisy synthetic signal where the artifacts at the left of the signal window have been rescaled by a factor of four for visualization purposes. (b) Same reconstruction when considering a projection of each iteration result into the signal space.

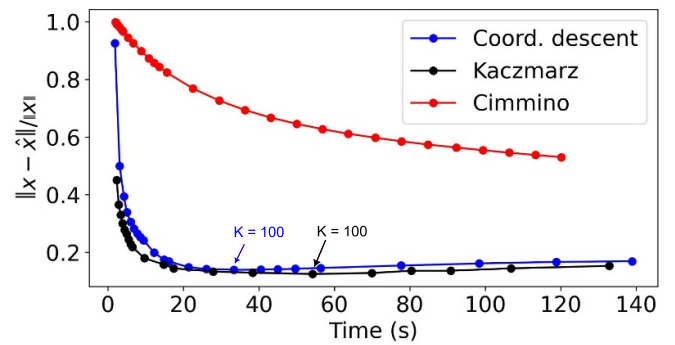


Figure 7. Evolution of the error as a function of time showing the convergence of each algorithm for the noisy synthetic inversions.

continuing to iterate may not improve the proposed solution $x^{(k)}$, so it is common to use a criteria to stop the calculations. This is addressed in more detail in section 6.

5. Fidelity map

To study the effect of noise on tomographic reconstructions, we developed a fidelity map. It quantifies how accurately a delta-like feature in the pinhole velocity-space can be reconstructed depending on its position within the domain and the noise level. As such, it serves as a diagnostic tool for evaluating the performance and reliability of the inversion technique. By visualizing fidelity maps for different noise levels, one can identify regions where the reconstruction is more or less accurate, thereby gaining insight into the effectiveness and limitations of the method.

The calculation process is the following. First, select a region of the pinhole's grid where the fidelity map is going to be built. Its grid resolution will be the same as the one stored in the weight matrix. For our case: $\rho \in [7, 16]$ cm and $\alpha \in [35, 70]$ degrees with resolution 1° in pitch angle and 0.1 cm in gyroscale. Then select an algorithm and a number of maximum iterations and set the percentage of background and

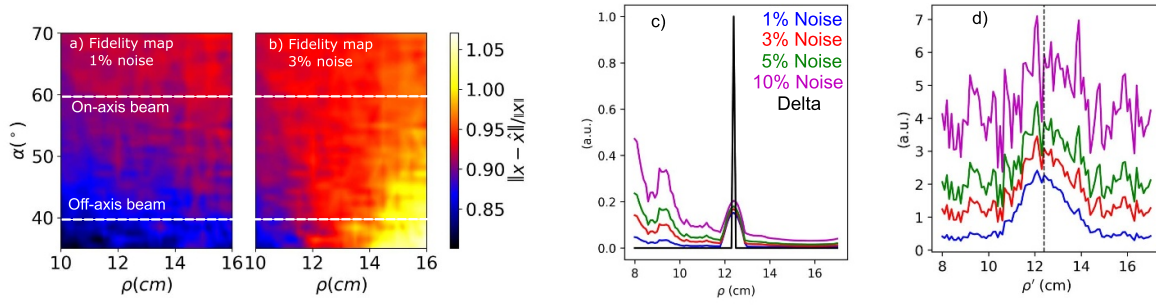


Figure 8. Fidelity maps for Kaczmarz, $k = 100$ iterations, 10% signal noise and 1% background noise in (a) and 3% background noise in (b). (c) 1D gyrospectral profiles of reconstruction examples for a delta placed at 12.4 cm and 60° with 10% signal noise and different levels of background noise. (d) shows the scintillator signal profiles corresponding to inversions in (c).

signal noise. Based on the performance of the three algorithms in section 4.2, the fidelity map is going to be built for the Kaczmarz using 100 iterations with 1% of background noise and 10% of signal noise. A delta is placed at a point on the grid selected in the first step. The synthetic measurements of this delta are later computed and reconstructed. Finally, the error ε is calculated to evaluate the reconstruction error. The process of placing and reconstructing deltas is repeated for every point of the grid defined at the beginning. To avoid the appearance of artifacts in the result, a projection to the signal region has to be made. However, the position of the delta is going to change, and to be able to compare reconstructions, it would be ideal to project all of them to the same region. Hence, a unique signal window must be applied for all deltas. All reconstructions will be projected to the space where the artifacts do not appear. The window chosen for projection is $\rho \in [6.5, 18]$ cm and $\alpha \in [30, 75]$ degrees.

The fidelity map generated with the parameters described in this section is shown in figure 8(a). An alternative fidelity map, where the background noise level has been artificially increased to 3%, is shown in figure 8(b).

In figure 8(a) it can be observed that the reconstruction error is lower when the delta sources are placed at a pitch angle of approximately 40° than when placed at 60° . This behavior is attributed to a slight broadening of the reconstructed peak in the gyroscale direction for higher pitch angles, which would correspond to on-axis NBI signals. Recent investigations show that 60° typically corresponds to trapped particles, whereas 40° are generally passing. The hypothesis is that the off-axis NBI, which has more edge-localized injection, populates a wider region of velocity space, and therefore results in both trapped and passing particles [54].

When comparing this fidelity map to the one corresponding to 3% of noise level (figure 8(b)), a general increase in reconstruction error is observed across the entire domain. This highlights the sensitivity of the tomographic technique to the noise present in the input signals. Figure 8(c) presents reconstructions integrated in pitch angle for a delta located at $\rho = 12.4$ cm

and $\alpha = 60^\circ$, which corresponds to the position of the on-axis NBI first-energy. Figure 8(d) shows the associated scintillator profile in gyroscale calculated by integrating the scintillator signal in pitch angle. At a 3% noise level, the maximum of the integrated reconstructed signal no longer coincides with the true delta position but instead shifts to a position inside the background noise region. This effect becomes even more pronounced at 5% and 10% noise. Nevertheless, it should be noted that the input peak is visible in all the reconstruction in the correct range of gyroscale. This proves the robustness of the algorithm, even under significant levels of noise present.

6. Stopping criteria

As established in section 4.2, iterative reconstructions exhibit semi-convergence, so the iteration count is treated as the regularization parameter and determined with the Resolution Principle, a criterion recently developed and validated for FILD reconstructions on ASDEX Upgrade [29]. The Resolution Principle uses pre-computed, noise-dependent resolution maps, Σ_ρ and Σ_α , to ensure that reconstructed signals remain separated by at least the local resolution; the optimal iterate k_0 is the largest k that still respects these limits. Methodological details (construction of the resolution maps, peak detection, decision rule, and comparisons to L -curve/discrepancy principle/normalized cumulative periodogram) are given in [29]; here we focus on MAST-U. For MAST-U, we compute the resolution maps using the Kaczmarz algorithm and a noise model mimicking the experimental data (10% signal, 1% background noise) and refine the pitch grid to 0.5° to match the experimental remap. The resulting maps (figure 9) select $k \simeq 200$ for the synthetic case (figure 10) and $k = 173$ for the experiment (section 7), suppressing sub-resolution splitting while preserving resolved structure. The resolution maps show the expected trend of worsening gyroscale resolution (a larger Σ_ρ) at larger ρ

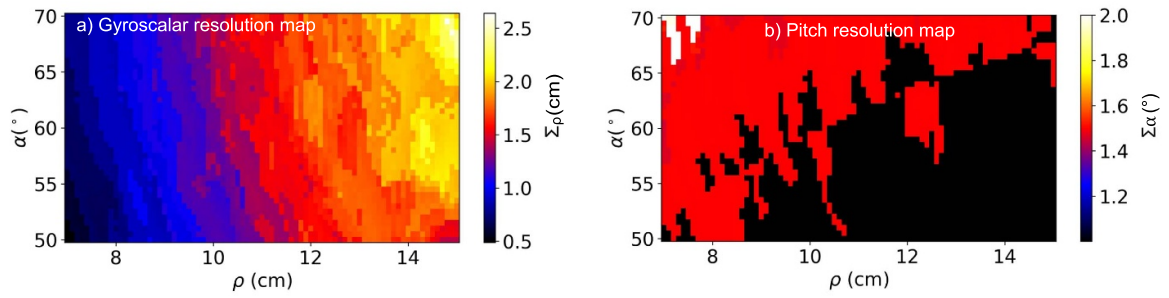


Figure 9. (a) Gyroscalar resolution map. (b) Pitch angle resolution map. Both calculated with Kaczmarz for $k = 100$ iterations, 1% background noise and 10% signal noise.

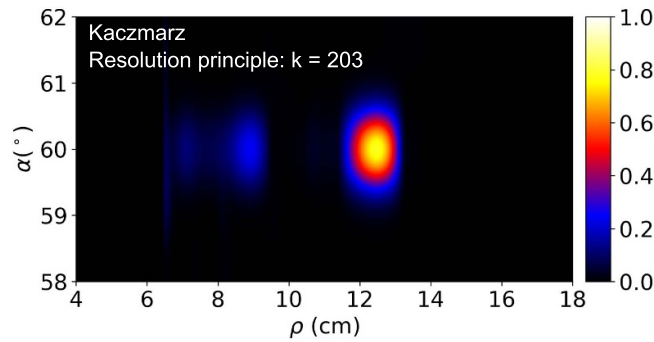


Figure 10. Kaczmarz reconstruction for $k = 203$, stopped by the resolution principle.

values, which is consistent with the known behavior of the intrinsic resolution of the diagnostic [40].

7. Inverse problem: experimental case

As indicated in section 4, the tomographic algorithms developed in this work are applied to an experimental signal corresponding to shot #47132 for $t = 0.30$ s. It corresponds to prompt losses of an L-mode plasma with 1.5 MW of on-axis NBI. The main injection energy is $E = 62.8$ keV. As in [40] it is assumed an homogeneous field to analyze the experimental data, the same approach is followed here for consistency. The instrument response from FILD is calculated assuming that the magnetic field does not vary in the FILD head. As the field on the pinhole is larger than the average field seen by the particles within the detector head, by approximately 3%–5%, this instrument response will overestimate the gyroscalar predicted by the inversion algorithms by the same amount.

In figure 11(a) the remap associated with the FILD measurements at that time is shown. As reference, a vertical line is included indicating the theoretical injection gyroscalar of the first energy of the NBI. The tails of the signal that extend towards larger gyroscalar are due to the finite resolution of the diagnostic.

Table 1. Centroids detected during the resolution principle algorithm.

ρ (cm)	α ($^\circ$)
10.1	73.0
12.4	69.0
12.7	58.0
12.8	63.3
13.3	57.0

The Kaczmarz algorithm has been applied to this experimental remap together with the resolution principle as stopping criteria. The optimal iteration according to this method is $k = 173$. The peaks detection algorithm localizes five components whose centroids are in table 1. Centroids associated with the point 12.7 cm and 58.0 $^\circ$ and the point 13.3 cm and 57.0 $^\circ$ trigger the stopping condition. Their separation in pitch angle is not above the pitch resolution at 12.7 cm and 58.0 $^\circ$ which is $\Sigma_\alpha = 1.5^\circ$ and their separation in gyroscalar is not sufficient to consider them independent. After the application of the iterative algorithm in figure 11 (b), the gyroscalar of the fast-ion population is much more well defined. The original remap presents a high spread of the signal in the gyroscalar direction. However, the dispersion is reduced by approximately 76%. To verify the fast-ion distribution obtained, the forward problem has been applied to this inversion in figure 11(c). Comparing this estimate with the actual data, it is seen that the four peaks can be recovered.

Three inversions of the same data performed using the non-negative Tikhonov 0th-order regularization are included in figure 12. Each one has a different value for its hyperparameter: 0.0008, 0.017 and 1.000. By comparing them, it can be observed how the choice of hyperparameter significantly affects the result. A small value returns a noisy and unreliable distribution, while if a higher value is chosen, the reconstruction becomes oversmooth. The L -curve method was used to determine which hyperparameter would be optimal. In particular, a scan of 10 logarithmically equally spaced values ranging from 10^{-4} to 1 has been performed. This should be $\lambda \sim 0.017$. However, it was not clear which value of λ should be taken as the curvature of the L -curve was not very pronounced.

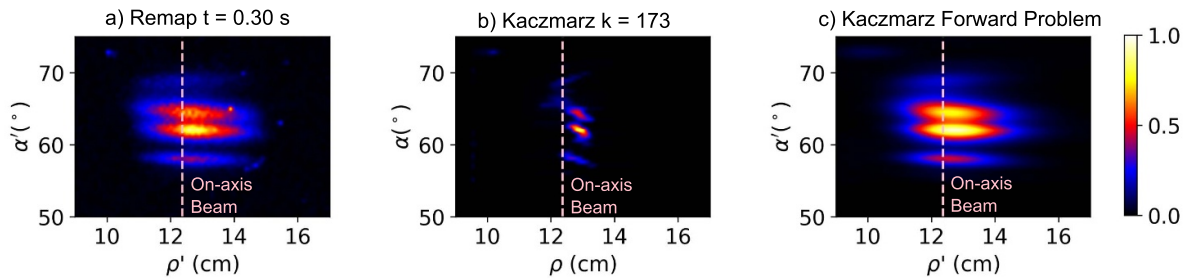


Figure 11. (a) Experimental remap to apply tomography to. (b) Tomographic reconstruction using Kaczmarz for $k = 173$ iterations using the resolution principle. (c) Forward problem applied to the iterative inversion performed by the coordinate descent.

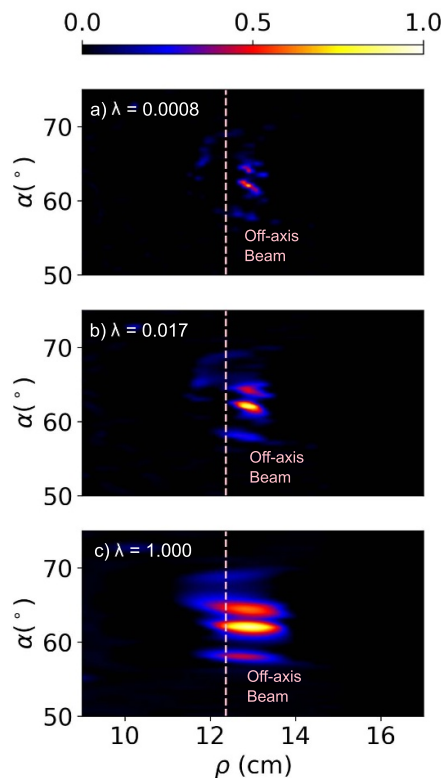


Figure 12. (a)–(c) correspond to Tikhonov inversions with hyperparameter values $\lambda = 0.0008, 0.017$ and 1.000 respectively.

The search for the hyperparameter is therefore a manual process that requires dedication and individualized treatment of each peak of each remap. In contrast, iterative algorithms have returned automatic results in seconds.

8. Conclusion and outlook

Building on the general methodology in [29] for reconstruction of velocity-space distribution functions of lost fast ions measured by FILDs, this work validates iterative reconstructions on the MAST-U FILD, a spherical-tokamak environment with a broader gyroradius range and more demanding resolution than AUG. On synthetic MAST-U cases, the Kaczmarz algorithm achieves the lowest reconstruction error, while coordinate descent offers the best time-per-iteration;

Cimmino converges too slowly for fast analysis in our setting. A fidelity map is introduced to quantify the reconstruction reliability and its sensitivity to noise across velocity space.

Applied to experimental MAST-U prompt-loss data (on-axis NBI, $t = 0.30$ s), the Resolution Principle selects $k = 173$ and yields a reconstruction with $\approx 76\%$ reduction of the ρ -dispersion, and forward projections that reproduce the four dominant peaks, demonstrating quantitative consistency with the measurement.

Operationally, the algorithms and stopping rule are implemented in FIELDSIM, enabling routine use on MAST-U. In future work, this framework will be extended to time-resolved analyses of fast-ion dynamics (e.g. ELM-driven acceleration) on MAST-U and other devices, leveraging the same stopping rule and tooling while adapting to device-specific resolution characteristics.










Data availability statement

The data cannot be made publicly available upon publication because they are not available in a format that is sufficiently accessible or reusable by other researchers. The data that support the findings of this study are available upon reasonable request from the authors.

Acknowledgments

This work has been carried out within the framework of the EUROfusion Consortium, funded by the European Union via the Euratom Research and Training Programme (Grant Agreement No. 101052200-EUROfusion) and from the EPSRC [Grant No. EP/W006839/1]. Views and opinions expressed are however those of the author(s) only and do not necessarily reflect those of the European Union or the European Commission. Neither the European Union nor the European Commission can be held responsible for them. Work performed by J. Rueda-Rueda and B. Schmidt is supported by US DOE under DE-SC0020337. This research received funding from the Plan Andaluz de Investigación, Desarrollo e Innovación (PAIDI 2020, No. 003456/A02W), Consejería de Transformación Económica, Industria, Conocimiento y Universidades de la Junta de Andalucía. The first author would like to thank J. Galdon-Quiroga for his guidance through this work.

ORCID iDs

M Jimenez-Comez  0009-0002-3037-206X
 B Schmidt  0000-0001-5302-9489
 J Rueda-Rueda  0000-0002-4535-326X
 L Velarde  0000-0002-3986-1583
 J F Rivero-Rodríguez  0000-0001-5074-0267
 A Reyner-Vinolas  0009-0000-5108-8194
 M Garcia-Munoz  0000-0002-3241-502X
 J Gonzalez-Martin  0000-0002-3237-5195
 E Viezzer  0000-0001-6419-6848

References

- [1] Garcia-Munoz M *et al* 2011 Fast-ion transport induced by Alfvén eigenmodes in the ASDEX Upgrade tokamak *Nucl. Fusion* **51** 103013
- [2] Pinches S D, Kiptily V G, Sharapov S E, Darrow D S, Eriksson L-G, Fahrbach H-U, García-Muñoz M, Reich M, Strumberger E and Werner A (The Asdex Upgrade Team and JET-EFDA Contributors) 2006 Observation and modelling of fast ion loss in JET and ASDEX Upgrade *Nucl. Fusion* **46** S904–10
- [3] Rivero-Rodríguez J F *et al* 2023 Transport and acceleration mechanism of fast ions during edge localized modes in ASDEX Upgrade *Nucl. Fusion* **63** 086028
- [4] Heidbrink W W and White R B 2020 Mechanisms of energetic-particle transport in magnetically confined plasmas *Phys. Plasmas* **27** 030901
- [5] Heidbrink W W 2008 Basic physics of Alfvén instabilities driven by energetic particles in toroidally confined plasmas *Phys. Plasmas* **15** 055501
- [6] Salewski M *et al* 2025 Energetic particle physics: chapter 7 of the special issue: on the path to tokamak burning plasma operation *Nucl. Fusion* **65** 043002
- [7] Galdon-Quiroga J *et al* (The ASDEX Upgrade Team and The EUROfusion MST1 Team) 2018 Velocity space resolved absolute measurement of fast ion losses induced by a tearing mode in the ASDEX Upgrade tokamak *Nucl. Fusion* **58** 036005
- [8] Garcia-Munoz M *et al* (The AUG and MST1 Teams) 2019 Active control of Alfvén eigenmodes in magnetically confined toroidal plasmas *Plasma Phys. Control. Fusion* **61** 054007
- [9] Zweben S J, Boivin R L, Diesso M, Hayes S, Hendel H W, Park H and Strachan J D 1990 Loss of alpha-like MeV fusion products from TFTR *Nucl. Fusion* **30** 1551–74
- [10] Rivero-Rodríguez J F *et al* 2018 A rotary and reciprocating scintillator based fast-ion loss detector for the MAST-U tokamak *Rev. Sci. Instrum.* **89** 10I112
- [11] Galdon-Quiroga J *et al* (The ASDEX Upgrade Team) 2018 Velocity-space sensitivity and tomography of scintillator-based fast-ion loss detectors *Plasma Phys. Control. Fusion* **60** 105005
- [12] Zweben S J, Darrow D S, Herrmann H W, Redi M H, Schivell J F and White R B 1995 Measurements of dt alpha particle loss near the outer midplane of tfr *Nucl. Fusion* **35** 1445
- [13] Darrow D S, Herrmann H W, Johnson D W, Marsala R J, Palladino R W, Zweben S J and Tuszewski M 1995 Measurement of loss of dt fusion products using scintillator detectors in tfr (invited) *Rev. Sci. Instrum.* **66** 476–82
- [14] García-Muñoz M, Fahrbach H-U and Zohm H (The ASDEX Upgrade Team) 2009 Scintillator based detector for fast-ion losses induced by magnetohydrodynamic instabilities in the ASDEX upgrade tokamak *Rev. Sci. Instrum.* **80** 053503
- [15] Gonzalez-Martin J *et al* (ASDEX Upgrade Team and MST1 Team) 2018 First measurements of a scintillator based fast-ion loss detector near the asdex upgrade divertor *Rev. Sci. Instrum.* **89** 10I106
- [16] Gonzalez-Martin J *et al* 2019 First measurements of a magnetically driven fast-ion loss detector on ASDEX Upgrade *J. Instrum.* **14** C11005–11005
- [17] Baeumel S *et al* (JET-EFDA Contributors) 2004 Scintillator probe for lost alpha measurements in JET *Rev. Sci. Instrum.* **75** 3563–5
- [18] Bonofiglio P J *et al* (JET Contributors) 2024 Alpha particle loss measurements and analysis in jet dt plasmas *Nucl. Fusion* **64** 096038
- [19] Rivero-Rodríguez J F *et al* (JET Contributors) 2021 Upgrade and absolute calibration of the jet scintillator-based fast-ion loss detector *Rev. Sci. Instrum.* **92** 043553
- [20] Fisher R K, Pace D C, García-Muñoz M, Heidbrink W W, Muscatello C M, Van Zeeland M A and Zhu Y B 2010 Scintillator-based diagnostic for fast ion loss measurements on DIII-D *Rev. Sci. Instrum.* **81** 10D307
- [21] Lee G S *et al* 2001 Design and construction of the KSTAR tokamak *Nucl. Fusion* **41** 1515–23
- [22] Kim J, Jun Young Kim S W Y, García-Muñoz M, Isobe M and Kim W C 2012 Initial measurements of fast ion loss in kstara *Rev. Sci. Instrum.* **83** 10D305
- [23] Chang J F, Isobe M, Ogawa K, Huang J, Wu C R, Xu Z, Jin Z, Lin S Y and Hu L Q (EAST Team) 2016 Scintillator-based fast ion loss measurements in the EAST *Rev. Sci. Instrum.* **87** 11E728
- [24] Wu C R *et al* (EAST Team) 2018 Performance of fast-ion loss diagnostic on east *Rev. Sci. Instrum.* **89** 10I144
- [25] Wang S 2023 Preliminary study of velocity-space distribution of fast-ion loss under ion cyclotron resonance heating in the east *Nucl. Tech.* **46** 120601
- [26] Poley J *et al* 2025 First microsecond velocity-space resolved simultaneous measurements of co- and counter-current fast-ion losses in forward and reverse magnetic field in a tokamak *Nucl. Fusion* **65** 076006
- [27] Stipani L 2021 A fast ion loss detector for the TCV tokamak *PhD Thesis* Lausanne, EPFL
- [28] Rivero-Rodríguez J F, Velarde L, Williams T, Galdón-Quiroga J, García-Muñoz M and McClements K G 2024 Initial operation of the scintillator-based fast-ion loss detector rotary and reciprocating system in MAST-U *IEEE Trans. Plasma Sci.* **52** 3878–84
- [29] Schmidt B S, Galdon-Quiroga J, Rueda-Rueda J, Poley-Sanjuán J, García-Muñoz M, Järleblad H, Reman B C G, Rud M, Valentini A and Salewski M (The ASDEX Upgrade Team and The EUROfusion Tokamak Exploitation Team) 2024 Iterative reconstruction methods and the resolution principle for fast-ion loss detector measurements *Nucl. Fusion* **64** 076009
- [30] Schmidt B S *et al* 2024 A new FILDSIM model for improved velocity-space sensitivity modelling and reconstructions *Plasma Phys. Control. Fusion* **66** 045004
- [31] Schmidt B S, Jorgensen J S, Rueda-Rueda J, Galdon-Quiroga J and García-Muñoz M and Salewski M (The ASDEX Upgrade Team) 2024 Anisotropic regularization for inversion of fast-ion loss detector measurements *Nucl. Fusion* **64** 106053
- [32] Galdon-Quiroga J *et al* (The ASDEX Upgrade Team and The Eurofusion MST1 Team) 2018 Beam-Ion Acceleration during Edge Localized Modes in the ASDEX Upgrade Tokamak *Phys. Rev. Lett.* **121** 025002
- [33] Galdon-Quiroga J *et al* (The ASDEX Upgrade Team and The EUROfusion MST1 Team) 2019 Observation of accelerated beam ion population during edge localized modes in the ASDEX Upgrade tokamak *Nucl. Fusion* **59** 066016

- [34] Kaczmarz S 1937 Angenäherte Auflösung von Systemen linearer Gleichungen *Bull. Int. Acad. Polon. Sci. Lett. Cl. Sci. Math. Nat.* **35** 355–7
- [35] Strohmer T and Vershynin R 2009 A Randomized kaczmarz algorithm with exponential convergence *J. Fourier Anal. Appl.* **15** 262–78
- [36] David W W 1994 Column-relaxed algebraic reconstruction algorithm for tomography with noisy data *Appl. Opt.* **33** 4420
- [37] Nesterov Y 2012 Efficiency of coordinate descent methods on huge-scale optimization problems *SIAM J. Optim.* **22** 341–62
- [38] Richtárik P and Takáč M 2014 Iteration complexity of randomized block-coordinate descent methods for minimizing a composite function *Math. Program.* **144** 1–38
- [39] Cimmino G 1938 Calcolo approssimato per le soluzioni dei sistemi di equazioni lineari *La Ricerca Sci.* **9** 326–33
- [40] Velarde L *et al* 2025 Velocity-space analysis of fast-ion losses measured in MAST-U using a high-speed camera in the FILD detector *Plasma Phys. Control. Fusion* **67** 015024
- [41] Rueda-Rueda J, Oyola P, Velarde L and Hidalgo-Salaverri J 2024 JoseRuedaRueda/ScintSuite: v1.3.10b First OpenSource (<https://doi.org/10.5281/zenodo.16709806>)
- [42] Rueda-Rueda J *et al* (ASDEX Upgrade Team) 2024 Commissioning of the imaging neutral particle analyser for the ASDEX Upgrade tokamak *Plasma Phys. Control. Fusion* **66** 035008
- [43] Salewski M *et al* 2012 Tomography of fast-ion velocity-space distributions from synthetic CTS and FIDA measurements *Nucl. Fusion* **52** 103008
- [44] Jacobsen A S, Salewski M, Eriksson J, Ericsson G, Korsholm S B, Leipold F, Nielsen S K, Rasmussen J and Stejner M (JET EFDA Contributors) 2015 Velocity-space sensitivity of neutron spectrometry measurements *Nucl. Fusion* **55** 053013
- [45] Salewski M *et al* (The ASDEX Upgrade Team) 2014 On velocity-space sensitivity of fast-ion D-alpha spectroscopy *Plasma Phys. Control. Fusion* **56** 105005
- [46] Jacobsen A S *et al* (The ASDEX Upgrade Team) 2016 Inversion methods for fast-ion velocity-space tomography in fusion plasmas *Plasma Phys. Control. Fusion* **58** 045016
- [47] Hansen P C 1998 Society for Industrial and Applied Mathematics *Rank-Deficient and Discrete Ill-Posed Problems: Numerical Aspects of Linear Inversion*
- [48] Hansen P C 2010 Society for Industrial and Applied Mathematics *Discrete Inverse Problems: Insight and Algorithms*
- [49] Natterer F 2001 Society for Industrial and Applied Mathematics *The Mathematics of Computerized Tomography*
- [50] Harrison J R *et al* 2024 Overview of physics results from MAST upgrade towards core-pedestal-exhaust integration *Nucl. Fusion* **64** 112017
- [51] Rueda-Rueda J, Garcia-Munoz M, Viezzer E, Schneider P A, Oyola P, Galdon-Quiroga J, Salewski M, Schmidt B S and Garcia-Dominguez J (ASDEX Upgrade Team) 2024 Tomographic reconstructions of the fast-ion phase space using imaging neutral particle analyser measurements *Plasma Phys. Control. Fusion* **66** 065025
- [52] Rueda-Rueda J 2024 JoseRuedaRueda/uFILD SIM: 4.bugFix June (<https://doi.org/10.5281/zenodo.16877774>)
- [53] Du X D, Gonzalez-Martin J, Liu D, Heidbrink W W and Van Zeeland M A 2023 Visualization of phase-space orbit topological boundary using imaging neutral particle analyzer *Nucl. Fusion* **63** 124002
- [54] Velarde L, *et al* Effect of $n = 2$ externally-applied magnetic perturbations on fast-ion confinement in MAST-U Submitted